The Astrophysical Journal, 829:78 (12pp), 2016 October 1 doi:10.3847/0004-637X/829/2/78

MAJOR-MERGER GALAXY PAIRS AT $Z = 0$: DUST PROPERTIES AND COMPANION MORPHOLOGY

Donovan L. Domingue[1], Chen Cao[2,3], C. Kevin Xu[3], Thomas H. Jarrett[4], Joseph Ronca[1], Emily Hill[1,5], and Allison Jacques[1]

[1] Georgia College & State University, CBX 82, Milledgeville, GA 31061, USA
[2] School of Space Science and Physics, Shandong University, Weihai, Weihai, Shandong 264209, China
[3] Infrared Processing and Analysis Center, California Institute of Technology 100-22, Pasadena, CA 91125, USA
[4] University of Cape Town, Private Bag X3, Rondebosch 7701, Republic of South Africa
[5] Specialty Analytical, 1711 SE Capps Road, Clackamas, OR 97015-6914, USA

Received 2016 March 22; revised 2016 July 11; accepted 2016 July 15; published 2016 September 23

ABSTRACT

We present an analysis of dust properties of a sample of close major-merger galaxy pairs selected by K_s magnitude and redshift. The pairs represent the two populations of spiral–spiral (S+S) and mixed morphology spiral–elliptical (S+E). The Code Investigating GALaxy Emission software is used to fit dust models to the Two Micron All Sky Survey, *Wide-Field Infrared Survey Explorer*, and *Herschel* flux density measurements, and to derive the parameters describing the polycyclic aromatic hydrocarbons contribution, interstellar radiation field, and photodissociation regions. Model fits verify our previous *Spitzer Space Telescope* analysis that S+S and S+E pairs do not have the same level of enhancement of star formation and differ in dust composition. The spirals of mixed-morphology galaxy pairs do not exhibit the enhancements in interstellar radiation field and therefore dust temperature for spirals in S+S pairs in contrast to what would be expected according to standard models of gas redistribution due to encounter torques. This suggests the importance of the companion environment/morphology in determining the dust properties of a spiral galaxy in a close major-merger pair.

Key words: galaxies: evolution – galaxies: interactions – galaxies: ISM – galaxies: spiral

1. INTRODUCTION

The Interstellar Medium (ISM) of spiral galaxies is composed of dust and gas at a multitude of temperatures as a result of the stellar life cycle. The various temperature states of the ISM along with H II regions (ionized hydrogen) provide an essential connection for understanding the evolution of galaxies due to their interaction with the radiation from young massive stars. Graphites and silicates from 0.01 to 0.2 μm in size compose the diffuse medium or cirrus that surrounds the star-forming H II regions (Mathis et al. 1977; Draine & Lee 1984; O'Donnell & Mathis 1997). While large dust grains obtain thermal equilibrium and exhibit a peak emission at wavelengths ~100–300 μm, smaller grains such as polycyclic aromatic hydrocarbons (PAH) grains are transiently heated by single photons and emit into the mid-infrared ~3–30 μm wavelengths with particularly strong emission features in the 6–12 μm wavelength range (Helou et al. 2000; Draine & Li 2007). The large grain dust mixture is heated by both the interstellar radiation field (ISRF), leading to cirrus temperatures ~20 K as well as the light from the star-forming regions yielding a higher temperature dust component (Xu & Helou 1996; Dale et al. 2012). Creation of the higher temperature dust component occurs at the interface of the densest ISM component, the molecular clouds, and the ionized H II regions known as the photodissociation regions (PDRs). The contribution of the PDR to the dust temperature is shown to be larger than that of previous studies after inclusion of *Herschel Space Telescope* (Pilbratt et al. 2010) data in the dust temperature analysis of KINGFISH survey galaxies (Dale et al. 2012). Studies of star-forming regions such as the Small Magellanic Cloud show a dependance of the PAH feature strengths on the ISRF intensity (Contursi et al. 2000). Galaxies with increased specific star formation rates (SFRs) may destroy PAH molecules (Engelbracht et al. 2005; Madden et al. 2006; Cook et al. 2014). Other causes of PAH destruction or absence have been attributed to metallicity effects (Engelbracht et al. 2005) and the presence of an active galactic nucleus (AGN; Roche et al. 1991), while Alonso-Herrero et al. (2014) observe that PAH grains were not destroyed in six AGN systems in which the grains are possibly protected by high gas column densities in galaxy nuclei.

An important step in the process of potential evolution of galaxy ISM is the pairing of galaxies. Galaxy pairs are an initial step in the eventual merger of the two galaxies. The universe is composed of galaxies that have been undergoing this assembly process over the Hubble time (Kauffmann et al. 1993; Cole et al. 2001). The result is an effective change in the galaxy count with an ever-increasing distribution to larger mass representatives of galaxies (Bundy et al. 2004, 2009). SFR and therefore the ISM evolve during mergers (Brinchmann et al. 1998; Xu et al. 2012) as well as when the pair companions are in a pre-merger stage of interaction with SFR exhibiting an anti-correlation with close proximity (Xu & Sulentic 1991; Barton et al. 2000, 2007; Scudder et al. 2012). The gravitational influence of galaxy interactions was first theorized by Toomre & Toomre (1972) and observationally shown in Larson & Tinsley (1978). These processes may occur as gas is redistributed both in location and ISM phase by the gravitational interaction that takes place during the encounter (Kennicutt et al. 1987; Dasyra et al. 2006; Hopkins et al. 2006). The standard model for gas redistribution is of a tidal torque delivering gas to the galaxy nucleus as in the simulations of Di Matteo et al. (2008). Merging galaxies have increased velocity dispersion in their ISM (Elmegreen et al. 1995). The increase in dispersion is dominated by supersonic gas turbulence in the cold star-forming phase of the ISM (Burkert 2006). Turbulence and substructure induced in the ISM during galaxy mergers (see Bournaud 2011 for a review) are now an additional mechanism for star formation investigated through simulations (Renaud et al. 2014).

The KPAIR sample of galaxy merger candidates was created in Domingue et al. (2009) to establish a baseline of merger stage properties solely based on the galaxies' physical proximity to each other. A key difference is that our sample will contain pairs in early and late stages of the galaxy–galaxy interaction while morphologically selected samples (Conselice et al. 2003; Darg et al. 2010) will be biased to actively distorted and changed systems. The choice of the galaxy sample location as the "local" nearby universe lets us resolve the pairs into separate galaxies. Studies of distant systems are not always capable of making this distinction and our study can serve as a baseline for high-redshift population studies. Two major types of galaxies, spirals (S) and ellipticals (E), are represented in the pair sample. Three possible pair combinations are S+S, S+E, and E+E. We have omitted the E+E option from further study as it does not represent a likely candidate for star formation enhancements due to lower relative ISM abundance. The KPAIR sample has been refined in an effort to understand the star-forming properties in the observing campaigns of Xu et al. (2010) and Cao et al. (2016) resulting in the current H-KPAIR sample examined in this paper.

Cao et al. (2016) demonstrate that the spirals in S+S pairs show significant enhancement in sSFR and star formation efficiency (SFE) while spirals in S+E pairs do not exhibit these enhancements. Xu et al. (2012) also find no significant sSFR enhancement in massive S+E pairs at any redshift. Other authors have shown this absence of SFR enhancements in S+E pairs and low SFR of spirals with early-type neighbors (Park et al. 2008; Park & Choi 2009; Hwang et al. 2011; Moon & Yoon 2015). Park et al. (2008) suggest the hot X-ray halo of early-type companions interacts hydrodynamically and deprives their paired spirals of cold gas and reduces SFRs. Another possible scenario for the relative lack of SFE enhancement in spirals of S+E pairs is the role of intrinsic interaction differences resulting from a disk–disk collision/ISM turbulence versus the single disk encounter. The likely unique merger history of a mixed-morphology pair (i.e., past major merger resulting in the early type) may include both of these scenarios. The available data from our IR studies allow us to further probe the properties of the dust component in the ISM of each population.

We describe the sample characteristics chosen to examine the dust properties in these close major-merger pairs populations and their relation to the star formation properties presented in Cao et al. (2016). Cao et al. (2016) present the far-infrared (FIR) data used in the present analysis but concentrate on the derivation of SFR and dust mass as an indication of gas content with the fitting models of Draine & Li (2007; DL07). In this present work we take the further steps of adding the near- and mid-infrared data to the analysis in order to understand the PAH contribution fractions and dust characteristics such as incident radiation intensity for both the pair and control samples. To describe our conclusions we first present the observations and data analysis required to create the flux density input to the SED models. Finally, we present the best-fit models and an analysis of their parameter correlations with the previously derived physical properties of the corresponding galaxies.

2. SAMPLE SELECTION

The galaxy pair sample was created from matching the SDSS DR5 (Adelman-McCarthy et al. 2007) spectroscopic galaxy catalog with the Two Micron All Sky Survey (2MASS) Extended Source Catalog (XSC; Jarrett et al. 2000) as described in Domingue et al. (2009). The matched catalog created a list of candidate pairs for which redshift ($\Delta v < 1000\,\mathrm{km\,s^{-1}}$), separation r, ($5\ \mathrm{h^{-1}\,kpc} \leqslant r \leqslant 20\ \mathrm{h^{-1}}$ kpc), and mass ($\Delta K_s < 1$; mass ratio $\leqslant 2.5$) are restricted to limit the sample to physical pairs complete to $K_s = 12.5$. *Spitzer Space Telescope* observations and analysis of a subsample of this final set of 170 major-merger pairs is presented in Xu et al. (2010). Here as in Cao et al. (2016) we begin with the *Herschel* subset (H-KPAIRS) sample developed by further restricting the selection of pairs with three criteria: (1) keep only pairs where both pair members have spectroscopically confirmed redshifts to avoid false pairs, (2) remove elliptical+elliptical pairs to facilitate the study of star-forming galaxies, and (3) keep only pairs with recession velocity $v > 2000\,\mathrm{km\,s^{-1}}$. The resulting H-KPAIR sample contains 88 galaxy pairs (44 are Spiral+Spiral (S+S) and 44 are Spiral+Elliptical (S+E)) with a median redshift $z \sim 0.04$.

The control galaxy sample was chosen from the *HerMES* survey (Oliver et al. 2012) for its *Herschel* coverage. It is selected based on matching morphology and stellar mass to the members of the H-KPAIR sample (Cao et al. 2016). *HerMES* (Bootes, EGS, ELAIS N1, Lockman SWIRE) field galaxies with companions at a projected distance of <70 kpc and $\Delta M_{\mathrm{star}} < 0.4$ dex were rejected along with peculiar and low-coverage (image edge) galaxies as an initial generation of the parent candidates . Spiral galaxies (morphology as in Cao et al. (2016)) were matched to pair members when $\Delta M_{\mathrm{star}} < 0.1$ dex. Although the control galaxies were not selected to match in redshift, the final one-to-one choice of the closest redshift galaxy to the pair member allows for the final control sample to have a mean redshift within the standard deviation of the H-KPAIR sample. The H-KPAIR mean $z = 0.037 \pm 0.013$ while that of the control is $z = 0.049 \pm 0.014$. A similar comparison of the stellar mass confirms the mass match with a mean $\log(M_{\mathrm{star}}) = 10.67 \pm 0.33$ and 10.66 ± 0.34 for the pair and control samples, respectively.

3. DATA FOR PAIRS

The implementation of the DL07 models requires a range of photometric measurements to develop an SED from the near- to mid-infrared for our galaxy samples. This section describes the data gathered from the surveys including 2MASS (Skrutskie et al. 2006) and the *Wide-field Infrared Survey Explorer* (*WISE*: Wright et al. 2010) as well as the *Herschel Space Observatory* (proposal ID: OT2_cxu_2) during which the pairs were observed in all six photometry bands from both *Herschel*/PACS (Poglitsch et al. 2010) and *Herschel*/SPIRE (Griffin et al. 2010) instruments.

3.1. 2MASS Data

2MASS (Skrutskie et al. 2006) observed the sky in the near-infrared at J (1.25 μm), H (1.65 μm), and K_s (2.16 μm) bands, which led to the development of 2MASS XSC. The original selection catalog of the sample pairs was developed with the magnitudes derived from XSC while the pairs with separations of less than 30″ required the deblending techniques of profile fitting and subtraction applied in Domingue et al. (2009). Both the catalog and profile fit magnitudes use the K_{20} value for the K_s-band magnitude (Jarrett et al. 2000). The resulting K_s-band

photometry is included in our SED fits as a baseline for the stellar contribution to the mid-infrared.

3.2. WISE Photometry and Calibrations

Mid-Infrared catalog photometry and images were extracted from the *WISE* mission archives from images of the sky at four infrared wavelengths (3.4, 4.6, 12, and 22 μm). Reprocessing the *WISE* "Atlas" imaging to achieve improved resolution was a necessary step to reduce the blending of the small separation galaxy pair members. The *WISE* Imaging Point-Source FWHM is reduced from 11.″4 and 18.″6 to 3.″5 and 5.″5 at 12 μm(*W*3) and 22 μm(*W*4), respectively, using the MCM-HiRes (Masci & Fowler 2009) techniques of Jarrett et al. (2012).

WISE photometry on the H-KPAIRS sample was done as either standard aperture photometry or model fitting due to galaxy pair member overlap and blending. Aperture photometry was performed with Aperture Photometry Tool (APT; Laher 2012) when pairs were widely separated compared to the extended flux of the pair members. Annuli larger than each aperture were used for sky background determination and subtraction. Pixel masking within APT was incorporated when the companion galaxy occupied part of the appropriate sized annuli. Zero-point flux calibration and modifications to the error estimates are based on the guidelines in the Explanatory Supplement to the *WISE* Preliminary Data Release Products.[6] When aperture photometry of the individual galaxies was not possible due to blending of the galaxies in a pair, aperture photometry was first applied to the entire pair and model fitting photometry was performed with IMFIT (Erwin 2015) in order to retrieve the relative deblended flux density of each galaxy. Moffat model fits were adequate in matching the galaxy profiles in the *WISE* bands. The relative flux density of each galaxy is fairly robust to the parameter adjustments. Total aperture flux density of the pair was divided based on relative IMFIT results. Errors are based on the area-dependent background error estimation. Aperture corrections for extended sources of 0.97 and 1.03 are applied to the *W*3 and *W*4 bands, respectively, as recommended in Jarrett et al. (2013). Color corrections are not applied to the flux density determination as the Code Investigating GALaxy Emission (CIGALE) code (Noll et al. 2009; Ciesla et al. 2014) via its python implementation (Roehlly et al. 2014) incorporates the *WISE* filter transmission curves as well as the transmission curve of each band contributing to the measured SED. Photometric errors are the quadratic sum of background subtraction error and the rms error as calculated in Dale et al. (2012) with a modification to include the correlated noise. This noise-variance correction factor ($F_{\rm corr}$) has a dependance on aperture radius specific to the *W*3 and *W*4 bands. The calibrations are based on the larger co-add pixels and conversions were made to HiRes pixels in the determination of the appropriate $F_{\rm corr}$ for each aperture. With an assumption that background error is random, the modified error is

$$\sigma = \sigma_{\rm sky}\,(F_{\rm corr})^{\frac{1}{2}}\left(N_{\rm ap} + \frac{N_{\rm ap}^2}{N_{\rm bk}}\right)^{\frac{1}{2}}, \quad (1)$$

[6] http://wise2.ipac.caltech.edu/docs/release/prelim/expsup/wise_prelrel_toc.html

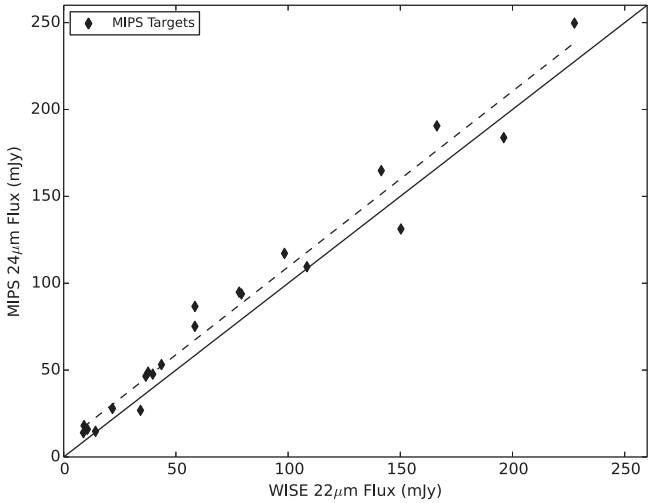

Figure 1. Comparison of MIPS 24 μm and *WISE W*4 22 μm photometry for 22 targets in common with Xu et al. (2010) The solid line represents a one-to-one match of the flux density and the dashed line is the best fit to the data.

where $\sigma_{\rm sky}$ is the background uncertainty and $N_{\rm ap}$, $N_{\rm bk}$ are the number of pixels in the aperture and background annulus, respectively.

As a check on the validity of the *W*4 (22 μm) photometry, we compare the measured flux density to that of the *Spitzer*/MIPS (Rieke et al. 2004) photometry for the pairs, which were also a part of the *Spitzer* KPAIR study (Xu et al. 2010). Figure 1 displays the result of the comparison. Considering the 2 μm wavelength difference of the flux density measures, the *W*4 values are consistent in a comparison to the MIPS flux densities (Xu et al. 2010).

3.3. Herschel Observations

Photometry for the galaxy pairs was performed (Cao et al. 2016) in six photometry bands from both *Herschel*/PACS (70, 100, 160 μm; Poglitsch et al. 2010) and *Herschel*/SPIRE (250, 350, 500 μm; Griffin et al. 2010) instruments. *Herschel*/PACS data were reduced with the application of UNIMAP (Traficante et al. 2011) to the HIPE (Ott 2010) archived data. PACS map pixel sizes are 3.″2 at 70 and 100 μm and 6.″4 at 160 μm. *Herschel*/SPIRE observations were reduced through HIPE 10.0.0 de-striper with standard SPIRE pipelines. SPIRE pixel sizes are 6″, 10″, and 14″ with beam FWHM of 18.″2, 24.″9, and 36.″3 for the 250, 350, and 500 μm images, respectively.

PACS and SPIRE photometry were performed through the use of aperture and background annulus flux density measures with APT Laher (2012) or IDL code when pairs did not exhibit blending. Photometric errors are taken as a quadratic sum of the background subtraction error and rms error. Pairs that were blended had a two-step photometry procedure with the initial use of IMFIT (Erwin 2015) to complete a simultaneous two-component fit to the galaxy profiles. Exponential disks and Gaussian fits were adequate to minimize model subtractions in PACS data while SPIRE data were reduced with PSF or two-dimensional Gaussian models. In the PACS procedures as in the *WISE* photometry, large apertures on the entire pair are used to determine the combined flux density while the IMFIT models determine the relative contribution of each pair member.

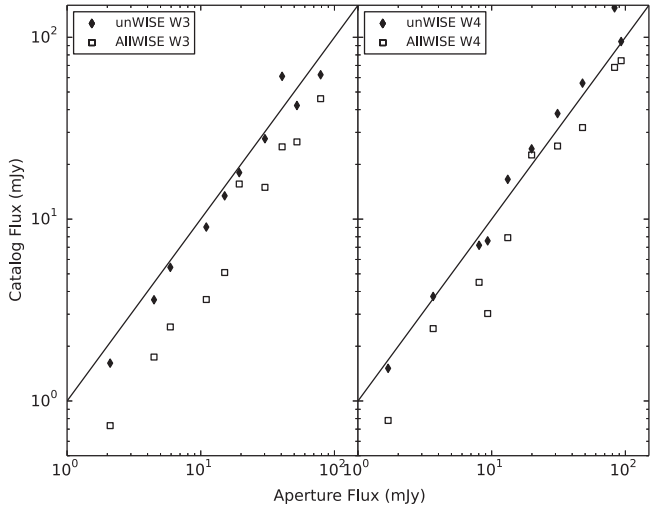

Figure 2. (Left) *WISE W*3 flux densities from unWISE and allWISE catalogs compared to aperture flux density measures in this work. (Right) The same comparison for *WISE W*4 flux density measurements. The solid lines represent a one-to-one match of the flux density.

4. DATA FOR CONTROL SAMPLE

The lack of nearby neighbors for control sample galaxies simplifies the determination of their flux density in the same NIR–FIR bands used for the pair sample. Without the hindrance of pair blending, K_s magnitudes are taken from the 2MASS XSC. The AllWISE (Cutri et al. 2014) source catalog provides magnitudes for *W*3 and *W*4 bands; however, the catalog is optimized for point-source detection and allows for active deblending, which may split extended sources into two detections. An alternative AllWISE catalog magnitude for extended sources is the use of the gmagW* intended to use elliptical apertures derived from available 2MASS photometry. These magnitudes have been shown to underestimate the flux density in Cluver et al. (2014) while the choice of a single large aperture magnitude may not be appropriate for the varying size of the control galaxies in the *W*3 and *W*4 bands. Another source for catalog magnitudes derived from *WISE* data is the unWISE database of Lang et al. (2014) and Lang (2014), which uses forced photometry on objects identified in the SDSS-III Data Release 10 (York et al. 2000; Eisenstein et al. 2011). We conduct a test comparison of *WISE* aperture flux density as conducted for the pair sample against unWISE and AllWISE flux densities for 10 of our control galaxies chosen to span their flux density range logarithmically. The unWISE flux densities provide the best match to the aperture flux densities as seen in Figure 2. We have adopted the unWISE catalog flux densities for all control galaxies in the remaining CIGALE analysis.

Herschel data for the control sample are taken from the *HerMES* data release (v2) with 2″, 3″/pixel for PACS 100, 160 μm data and 6″, 8.″33, and 12″/pixel for SPIRE 250, 350, and 500 μm, respectively. Photometry was derived on these images (Cao et al. 2016) with circular or elliptical apertures using IDL/phot. Background and photometric errors were determined from the aperture annuli.

5. SAMPLE CHARACTERISTICS

We limit our candidates for SED analysis to the 132 spiral galaxies as representatives of a dust-rich star-forming population. In order to introduce available observation band uniformity to the SED analysis, we require that the spiral galaxies have PACS and SPIRE detections from 100 to 350 μm as well as *WISE* 22 μm and K_s detections. Both upper limits and detections are initially used as input in the additional 12, 70, and 500 μm bands for the galaxies meeting this criteria. The 70 μm data is not available for our control galaxies and subsequent flux density inputs only include *Herschel* data from 100 to 500 μm as discussed in section on SED fits. Based on the restriction, 47 spiral galaxies of the H-KPAIR sample are not included in our analysis. Of these excluded galaxies, 17 have been established to have log(sSFR) < -11.5 (Cao et al. 2016) with the implication that they are near the "red and dead" description of spirals. Another 15 only have an upper limit on SFR and the remaining 15 have missing flux density measures at *Herschel* bands determined as necessary for accurate dust property measurements.

6. DUST MODELS AND SED FITS

We use the python implementation of the SED fitting software known as the CIGALE (Noll et al. 2009; Roehlly et al. 2012, 2014) to derive the PAH emission characteristics of the *Herschel*-observed star-forming galaxies in a K_s-band selected galaxy pair sample (H-KPAIRS) Cao et al. (2016). The CIGALE code allows users to choose models for star formation history, single stellar populations, and dust emission, among other options, to incorporate into a best-fit procedure for the observed SED. We implement the Maraston (2005) stellar population model with a Kroupa (2001) initial mass function and a solar metallicity of $Z = 0.02$. The adopted star formation history model is composed of two decreasing exponentials with an e-folding time taken as a variable of 2 Gyr for "red and dead" spirals or 10 Gyr for active star-forming spirals allowing for the best fit. The star-forming history also allows a late burst mass fraction to vary between 0.001, 0.01, and 0.1. The dust model chosen here is the DL07 model as expanded in Aniano et al. (2012) to include a larger range of models known as the DL2014 models in CIGALE. The varied parameters of the Draine & Li (2007) models are qPAH, γ, and $U_{\rm min}$. The parameter qPAH represents the percentage of the dust mass composed of PAH with $< 10^3$ C atoms. The (1-γ) is the fraction of dust exposed to the ISRF described by $U_{\rm min}$, a dimensionless intensity factor. Other areas of the galaxy are exposed to an intensity factor $U \geqslant U_{\rm min}$ up to a maximum value of $U_{\rm max}$ following a distribution of heating intensities from $U_{\rm min}$ to $U_{\rm max}$ described by the DL07 power-law function

$$\frac{dM_{\rm dust}}{dU} = (1 - \gamma) M_{\rm dust}\, \delta(U - U_{\rm min}) + \gamma M_{\rm dust} \frac{\alpha - 1}{U_{\rm min}^{1-\alpha} - U_{\rm max}^{1-\alpha}} U^{-\alpha},\ \alpha \neq 1, \quad (2)$$

where $U_{\rm min} \leqslant U \leqslant U_{\rm max}$, δ is the Dirac delta function, which ensures the first term only contributes outside of the PDR, and $M_{\rm dust}$ is the total dust mass. Draine et al. (2007) indicate that the power α may be held fixed $\alpha = 2$ without affecting the quality of the fits to the SED of many galaxies and $U_{\rm max} = 10^7$ may also be set as a fixed parameter (Aniano et al. 2012). The minimum ISRF ($U_{\rm min}$) parameter is varied among all available values between $U_{\rm min} = 0.1$ to $U_{\rm min} = 50$. The qPAH model parameters are qPAH = 0.47, 1.12, 1.77, 2.50, 3.19, 3.90, 4.58, 5.26, 5.95, 6.63, and 7.32. The γ parameter as fraction of

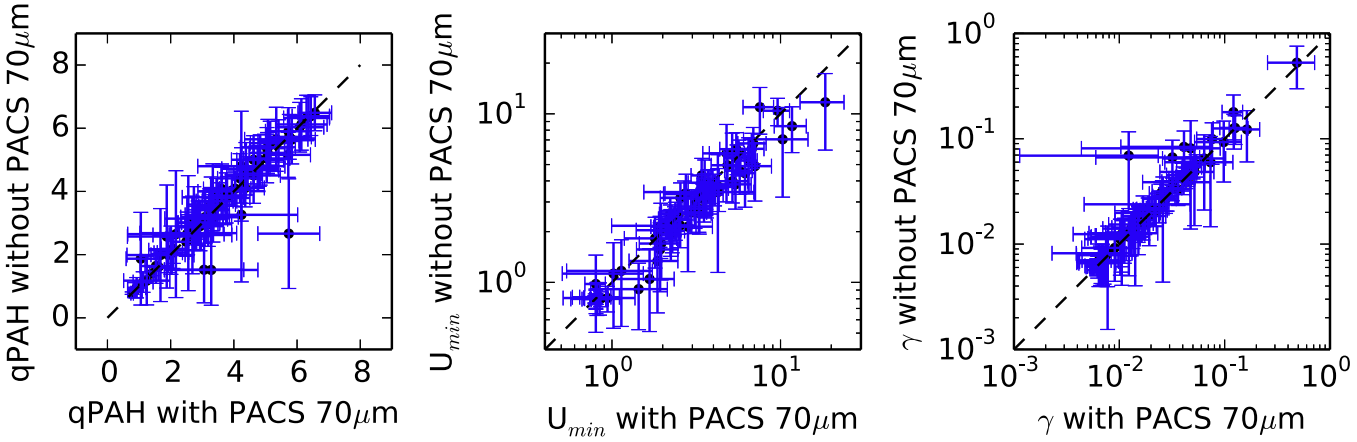

Figure 3. Comparison of the parameter results for qPAH, Umin, and γ from the use of CIGALE when including and excluding the available PACS 70 μm band as input. The dashed line represents a one-to-one match of the parameters. Error bars are from the probability distribution of each SED fit.

the galaxy is logarithmically spaced from 10^{-3} to 1.0. The redshift of each galaxy is applied to create rest frame SED fits.

Two other quantities descriptive of the dust conditions (Draine & Li 2007) are the $f_{\rm PDR}$, total dust luminosity that is emitted by the dust grains in regions with $U > 10^2$, and the mean starlight intensity $\langle U \rangle$. The $\langle U \rangle$ and $f_{\rm PDR}$ are defined as

$$\langle U \rangle = (1-\gamma)U_{\rm min} + \frac{\gamma U_{\rm min}\ln(U_{\rm max}/U_{\rm min})}{1 - U_{\rm min}/U_{\rm max}} \quad (3)$$

and

$$f_{\rm PDR} = \frac{\gamma \ln(U_{\rm max}/10^2)}{(1-\gamma)(1-U_{\rm min}/U_{\rm max}) + \gamma \ln(U_{\rm max}/U_{\rm min})}. \quad (4)$$

The CIGALE code utlitlizes χ^2 minimization defined in Ciesla et al. (2014) to find the best DL07 model match to the photometry of each galaxy as

$$\chi^2(a_1,\ldots,a_i,\ldots,a_N) = \sum_i^M \left[\frac{y_i - \eta y(x_i, a_1,\ldots,a_i,\ldots,a_N)}{\sigma_i}\right]^2, \quad (5)$$

and the reduced χ^2 is

$$\chi^2_{\rm red} = \frac{\chi^2}{M-N}, \quad (6)$$

where the models are represented as y, the model parameters as a_i, the observations as x_i, and the observation errors are σ_i. There are N parameters and M number of data. The normalization η is obtained from

$$\eta = \frac{\sum_{i=1}^N y_i \times y(x_i, a_1,\ldots,a_i,\ldots,a_M)/\sigma_i^2}{\sum_{i=1}^N y(x_i, a_1,\ldots,a_i,\ldots,a_M)/\sigma_i^2}. \quad (7)$$

A probability distribution function (PDF) is created as each parameter is varied and $\chi^2_{\rm red}$ values are calculated. The minimum $\chi^2_{\rm red}$ for each discrete parameter is used to develop the distribution from which the mean and standard deviation are taken as the "estimated" value with its error. CIGALE reports the "best" parameter as the parameter taken from the model with the minimum $\chi^2_{\rm red}$. In this paper the "estimated" values obtained from the PDFs are used for the dust analysis with their errors taken from the PDF standard deviations.

Since the control sample does not have the PACS 70 μm flux density measurement as an input into the SED fit, we tested the derived parameters from our pair galaxy sample with and without the use of PACS 70 μm flux densities. The parameter values for qPAH, Umin, and γ derived from the full set of flux density measures are shown in Figure 3 to be within the errors of these same parameters when the PACS 70 μm is intentionally excluded from the fit with the exception of one galaxy fit. Due to the limits on the control sample, the CIGALE-derived parameter analysis will be restricted to both samples without the PACS 70 μm to increase the similarity of the precision on the determination of the best models.

Ciesla et al. (2014) demonstrate through the use of mock galaxy input, that missing 70 μm data does not affect the determination of qPAH or γ while $U_{\rm min}$ is possibly overestimated by 18%. Our analysis of $U_{\rm min}$ treats each of our samples without the 70 μm data and should present an accurate relative comparison of this dust parameter. The lack of the PAH 8 μm feature as a measurement in our analysis will not affect any of the DL07 parameters (Ciesla et al. 2014). Examples of the produced SED fits are shown in Figure 4.

7. CONTRIBUTIONS OF AGN

As active galactic nuclei could contribute to the *WISE* bands and the overall SED fits and confuse the flux density contribution from dust, an analysis of the *WISE* flux densities as potential indicators of AGN activity was conducted. *WISE* photometry (Jarrett et al. 2011; Mateos et al. 2012; Stern et al. 2012) has been used as a successful approach in AGN identification. A color criteria of Mateos et al. (2012), is applied using *W*1, W2, and *W*3 magnitudes taken from the unWISE forced photometry catalog (Lang 2014; Lang et al. 2014). In the catalog, apertures are determined based on SDSS photometry and are held constant for the *WISE* band measures. The forced photometry should be sufficient to measure the magnitude differences *W*1–*W*2 and *W*2–*W*3 for the placement of the H-KPAIRs in the *WISE* color–color diagram. From the full set of spirals in the H-KPAIRs, only J13151726+4424255 falls within the color–color diagram area associated with the AGN in Mateos et al. (2012) and therefore the unWISE photometry indicates that this may be our only AGN candidate. As a check on the catalog photometry analysis, additional manual aperture photometry is also carried out using APT on

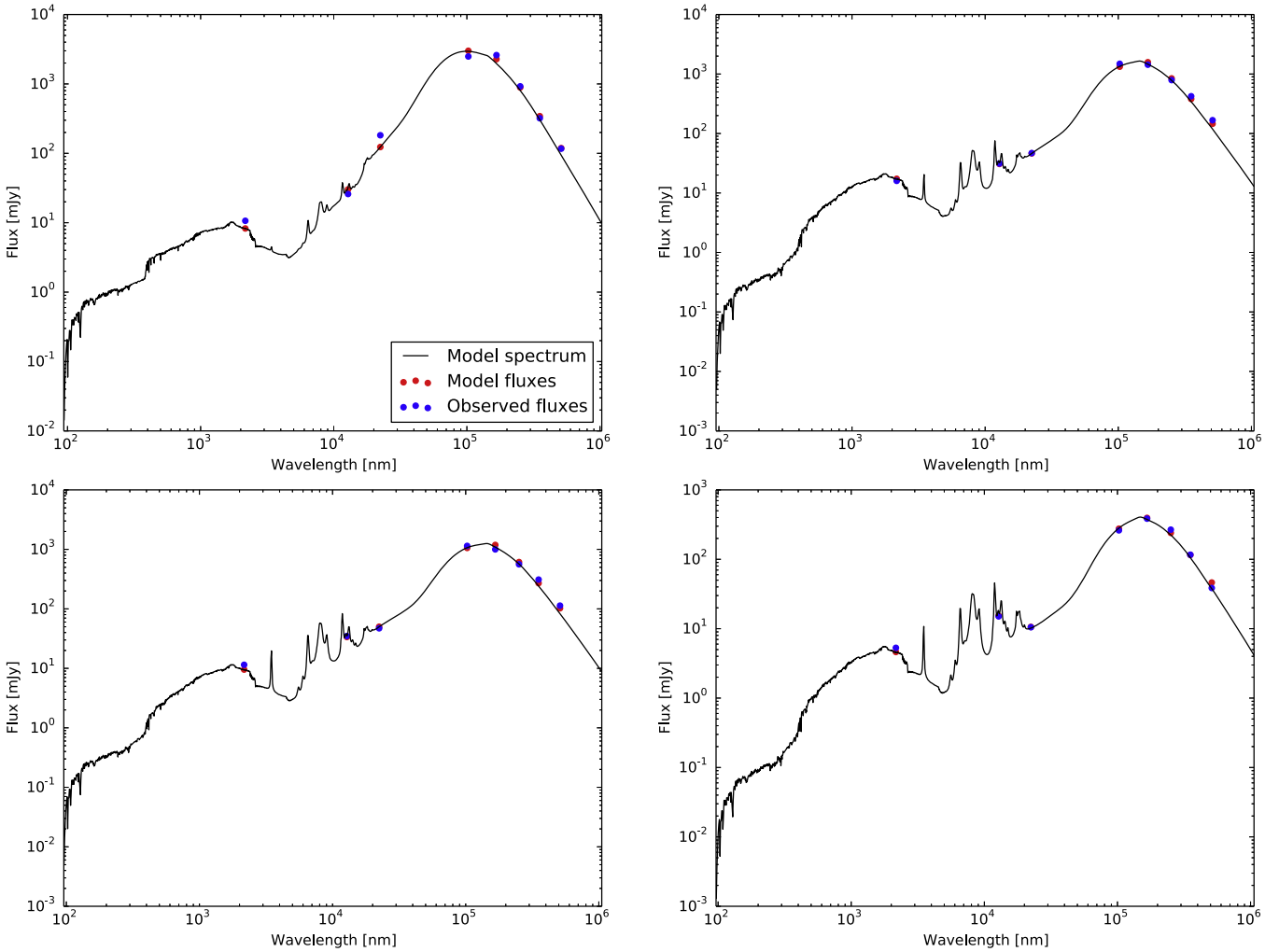

Figure 4. Example SED fits for galaxies with a range of qPAH values exhibited by the intensity of the model spectrum emission lines.

the *W*1 and *W*2 *WISE* imaging. Photometry was derived from the largest apertures allowed on the spirals, which did not extend to the blended or overlap regions of the pairs. While these apertures do not contain the total flux density of each galaxy in many cases, they are kept the same for both bands and certainly include the nuclear contribution to these mid-infrared flux densities. According to the *W*1–*W*2 criteria, two galaxies are identified as a potential AGN by means of the aperture photometry, J12115648+4039184, and as also identified in the preliminary test, J13151726+4424255. These two galaxies have the highest values of $\langle U \rangle$ and γ in the sample and can be visually identified as the outlier points in Figure 9. The $U_{\rm min}$ value of J13151726+4424255 is not unusual in the context of the reported $U_{\rm min}$ distribution. The galaxies occupy two different mass bins of our subsequent analysis and any bias to our conclusions due to their inclusion is minimized.

8. DISTRIBUTION OF DUST PARAMETERS

The output of our CIGALE model fits is listed in Table 1. Of the 85 spirals input into our model fits, 5 can be classified as poorly fit with $\chi^2_{\rm red} \geqslant 4$. The average $\chi^2_{\rm red} \sim 1$ for the pair sample. Three galaxies are poorly fitted from S+S and two are poorly fitted from S+E. Analysis of the output parameters is limited to galaxies with $\chi^2_{\rm red} < 4$. We similarly reject analysis of control galaxies with $\chi^2_{\rm red} \geqslant 4$. This leaves 67 control galaxies for a remaining analysis. The CIGALE-derived $L_{\rm dust}$ is consistent (see Figure 5) with the $L_{\rm IR}$ of Cao et al. (2016). Figure 6 displays the distribution of the $U_{\rm min}$, qPAH, and γ parameter output of CIGALE for the S+S, S+E, and control samples along with those of the calculated values of $\langle U \rangle$, the fraction of $L_{\rm dust}$ emitted from regions with $U > 10^2$ (known as fPDR), and $L_{\rm dust}$. A two-sided Kolmogorov–Smirnov (K–S) test (see Table 2) on the population distributions reveals that those of the spirals in S+S pairs are statistically different from the control sample for basic output parameters of $U_{\rm min}$, qPAH, and $L_{\rm dust}$. The distributions of the $U_{\rm min}$ and $L_{\rm dust}$ parameters for spirals in S+S are also different from their corresponding spirals in S+E. The qPAH distributions for the spirals in both pair morphology types differ at the $P = 0.15$ significant level. The γ parameter distributions show no significant differences across samples.

The calculated parameter distributions for $\langle U \rangle$ and fPDR also show a significant difference for S+S versus the control sample while they are only different from S+E spirals in the $\langle U \rangle$ parameter distribution.

Table 1
H-KPAIR Galaxy CIGALE SED Results

(1) Galaxy ID (2MASX)	(2) $\log(\mathrm{SFR}/M_{\mathrm{star}})$ yr^{-1}	(3) $\log(M_{\mathrm{star}})$ ($M\odot$)	(4) Type	(5) χ^2_{red}	(6) qPAH (%)	(7) γ (%)	(8) U_{min}	(9) $\langle U\rangle$	(10) $\log(L_{\mathrm{dust}})$ ($L\odot$)	(11) f_{PDR}
J00202580+0049350	−10.00	10.70	S+E	0.17	3.47 ± 0.55	1.21 ± 0.51	3.31 ± 0.61	3.87	10.10	0.12
J01183417−0013416	−9.23	10.98	S+S	0.51	1.13 ± 0.33	3.02 ± 0.68	8.45 ± 2.56	11.76	11.45	0.25
J01183556−0013594	−9.88	10.65	S+S	0.98	3.43 ± 0.66	0.82 ± 0.66	3.80 ± 0.86	4.22	10.72	0.08
J02110638−0039191	−9.98	10.45	S+S	0.46	3.41 ± 0.49	0.79 ± 0.39	3.81 ± 0.86	4.22	10.32	0.08
J03381222+0110088	−10.42	11.05	S+E	0.41	4.41 ± 0.78	1.21 ± 0.55	2.18 ± 0.57	2.55	10.51	0.12
J07543194+1648214	−9.85	10.08	S+S	2.16	3.53 ± 0.60	0.70 ± 0.30	5.28 ± 1.93	5.77	11.14	0.07
J07543221+1648349	−9.98	10.34	S+S	0.57	2.86 ± 0.55	1.13 ± 0.59	2.60 ± 0.66	3.02	10.98	0.11
J08083377+3854534	−10.17	11.16	S+E	1.27	4.51 ± 0.88	1.18 ± 0.67	5.83 ± 2.82	6.74	10.04	0.12
J08233266+2120171	−10.27	10.56	S+S	0.28	3.69 ± 0.72	3.41 ± 0.83	3.61 ± 0.77	5.32	10.14	0.27
J08233421+2120515	−10.38	10.69	S+S	0.57	3.01 ± 0.69	4.91 ± 1.19	3.68 ± 1.05	6.18	10.25	0.34
J08291491+5531227	−9.96	11.12	S+S	1.08	5.37 ± 0.65	0.60 ± 0.03	1.05 ± 0.54	1.14	10.29	0.06
J08292083+5531081	−10.31	10.93	S+S	0.82	5.40 ± 0.88	1.40 ± 0.63	0.91 ± 0.39	1.11	10.32	0.13
J08381759+3054534	−10.44	10.49	S+S	2.02	3.18 ± 0.79	2.10 ± 0.63	6.17 ± 1.56	7.89	10.51	0.19
J08390125+3613042	−10.27	10.59	S+E	1.56	5.60 ± 0.67	0.60 ± 0.03	0.80 ± 0.06	0.87	10.04	0.06
J09060498+5144071	−10.14	10.42	S+E	0.34	5.53 ± 0.70	0.60 ± 0.07	0.81 ± 0.14	0.88	9.95	0.06
J09134606+4742001	−10.30	10.35	S+E	0.39	6.03 ± 0.79	2.69 ± 0.74	2.17 ± 0.35	3.01	10.65	0.22
J09155467+4419510	−10.95	10.84	S+S	1.75	1.99 ± 0.56	5.38 ± 1.22	6.20 ± 1.46	10.63	11.25	0.36
J09155552+4419580	−10.49	11.19	S+S	1.60	1.40 ± 0.07	0.60 ± 0.03	10.43 ± 1.93	11.23	11.45	0.06
J09374413+0245394	−10.63	10.88	S+E	0.17	3.86 ± 0.61	1.29 ± 0.52	2.35 ± 0.46	2.78	10.76	0.13
J10100079+5440198	−10.39	9.84	S+S	0.16	4.67 ± 0.68	0.68 ± 0.28	2.28 ± 0.37	2.50	10.89	0.07
J10100212+5440279	−10.64	10.22	S+S	0.83	3.81 ± 1.06	1.27 ± 0.87	1.34 ± 0.68	1.59	10.38	0.12
J10205188+4831096	−10.20	10.12	S+E	0.35	2.41 ± 0.46	2.19 ± 0.60	3.36 ± 1.02	4.39	10.34	0.19
J10225647+3446564	−10.07	10.06	S+S	0.23	1.64 ± 0.55	5.52 ± 1.24	2.74 ± 0.75	4.87	10.64	0.36
J10233658+4220477	−10.75	10.16	S+S	1.73	2.63 ± 0.63	4.70 ± 1.18	3.22 ± 0.94	5.33	10.98	0.33
J10233684+4221037	−10.30	10.91	S+S	0.75	5.65 ± 1.01	1.24 ± 0.84	4.89 ± 1.86	5.71	10.46	0.12
J10272950+0114490	−10.81	10.98	S+E	0.56	4.73 ± 0.71	0.70 ± 0.30	4.95 ± 1.23	5.42	10.17	0.07
J10332972+4404342	−10.57	10.60	S+S	1.17	3.69 ± 0.58	1.69 ± 0.55	3.18 ± 0.77	3.92	10.92	0.16
J10333162+4404212	−10.51	10.86	S+S	1.41	3.12 ± 0.44	0.61 ± 0.09	3.34 ± 0.65	3.63	10.55	0.06
J10435053+0645466	−10.19	10.50	S+S	1.17	3.01 ± 0.71	5.69 ± 1.36	2.82 ± 0.73	5.07	10.66	0.36
J10435268+0645256	−9.78	10.81	S+S	0.99	4.80 ± 1.74	3.87 ± 3.91	0.79 ± 0.04	1.26	9.80	0.28
J10452478+3910298	−10.47	10.14	S+E	3.40	1.87 ± 1.47	12.26 ± 6.23	0.79 ± 0.04	2.29	9.80	0.49
J11065068+4751090	−10.03	10.48	S+S	0.25	5.90 ± 0.75	0.68 ± 0.28	3.13 ± 0.69	3.43	10.89	0.07
J11204657+0028142	−10.12	10.38	S+S	0.22	2.14 ± 0.76	9.95 ± 4.22	7.06 ± 3.85	16.30	9.71	0.50
J11251716+0226488	−9.65	10.67	S+S	1.09	1.52 ± 1.05	6.65 ± 3.03	0.81 ± 0.16	1.64	10.19	0.38
J11273289+3604168	−11.05	11.26	S+S	3.34	1.52 ± 1.12	8.37 ± 3.47	0.82 ± 0.18	1.86	9.83	0.42
J11273467+3603470	−9.70	10.96	S+S	1.21	5.73 ± 0.71	0.60 ± 0.06	2.28 ± 0.39	2.48	10.60	0.06
J11440433+3332339	−10.37	10.92	S+E	0.75	4.80 ± 0.64	0.62 ± 0.15	2.31 ± 0.57	2.51	9.97	0.07
J11484370+3547002	−10.07	11.15	S+S	0.52	2.68 ± 0.52	2.15 ± 0.66	2.04 ± 0.43	2.67	10.84	0.19
J11484525+3547092	−10.28	10.74	S+S	1.76	2.65 ± 2.01	5.99 ± 4.52	2.17 ± 0.78	4.03	10.83	0.37
J11501399+3746306	−9.32	10.74	S+S	1.75	6.12 ± 0.81	1.11 ± 0.61	2.02 ± 0.68	2.35	10.40	0.11
J12020424+5342317	−10.35	10.49	S+E	0.35	1.99 ± 1.47	9.29 ± 5.41	0.80 ± 0.11	1.94	10.12	0.44
J12115507+4039182	−9.47	11.11	S+S	0.74	2.62 ± 1.23	2.39 ± 1.95	5.82 ± 1.86	7.68	9.97	0.21
J12115648+4039184	−10.08	10.89	S+S	1.51	0.95 ± 0.32	17.89 ± 8.14	11.71 ± 5.62	38.23	10.63	0.63
J12191866+1201054	−10.58	10.71	S+E	0.67	4.00 ± 0.87	1.85 ± 0.88	2.02 ± 0.52	2.56	9.88	0.17
J12433887+4405399	−10.63	10.91	S+E	1.59	4.03 ± 0.50	0.60 ± 0.03	1.70 ± 0.67	1.85	9.99	0.06
J12525011+4645272	−10.50	10.60	S+E	1.54	1.18 ± 0.77	12.52 ± 4.55	0.82 ± 0.18	2.39	10.24	0.49
J13011662+4803366	−10.32	10.84	S+S	1.14	3.58 ± 0.87	4.52 ± 1.33	3.98 ± 1.02	6.45	10.56	0.32
J13011835+4803304	−9.91	10.66	S+S	0.86	2.66 ± 0.69	1.98 ± 0.89	4.60 ± 1.27	5.83	10.36	0.18
J13082737+0422125	−9.83	10.81	S+S	0.03	3.26 ± 2.12	8.11 ± 6.72	0.80 ± 0.06	1.79	9.34	0.42
J13082964+0422045	−9.97	10.55	S+S	0.15	2.68 ± 1.82	6.50 ± 4.39	0.80 ± 0.10	1.60	9.40	0.37
J13151386+4424264	−9.88	10.53	S+S	0.79	6.36 ± 0.67	0.82 ± 0.42	2.38 ± 0.60	2.66	10.45	0.08
J13151726+4424255	−10.67	10.42	S+S	0.36	3.14 ± 1.01	52.74 ± 22.91	3.43 ± 2.29	28.57	11.09	0.73
J13153076+6207447	−10.18	11.11	S+S	2.56	0.78 ± 0.04	1.57 ± 0.33	10.95 ± 3.38	13.13	10.89	0.15
J13153506+6207287	−10.92	10.97	S+S	6.58	0.79 ± 0.07	3.46 ± 0.66	17.38 ± 3.23	24.76	11.35	0.28
J13325525−0301347	−10.05	10.94	S+S	0.99	2.06 ± 0.49	3.91 ± 0.91	3.81 ± 1.10	5.87	10.62	0.29
J13325655−0301395	−10.42	11.27	S+S	0.76	4.57 ± 0.53	0.60 ± 0.03	3.27 ± 0.67	3.55	10.57	0.06
J13462001−0325407	−10.80	10.63	S+E	4.37	6.59 ± 0.54	0.64 ± 0.19	1.03 ± 0.52	1.13	9.51	0.07
J14005783+4251203	−10.41	10.95	S+S	0.25	3.01 ± 0.52	2.11 ± 0.56	3.18 ± 0.66	4.11	10.63	0.19
J14005879+4250427	−10.37	10.40	S+S	0.91	2.07 ± 0.50	4.32 ± 0.96	5.63 ± 1.35	8.89	10.80	0.32
J14055079+6542598	−10.77	10.84	S+E	0.65	5.00 ± 0.76	0.70 ± 0.30	0.80 ± 0.08	0.88	9.67	0.07
J14062157+5043303	−9.97	10.15	S+E	0.23	5.64 ± 0.77	0.66 ± 0.24	3.77 ± 0.65	4.12	10.46	0.07
J14070703−0234513	−10.79	11.05	S+E	0.05	2.66 ± 1.74	6.91 ± 4.73	0.98 ± 0.47	2.00	10.40	0.39

Table 1
(Continued)

(1) Galaxy ID (2MASX)	(2) $\log(\mathrm{SFR}/M_{\mathrm{star}})$ yr^{-1}	(3) $\log(M_{\mathrm{star}})$ $(M\odot)$	(4) Type	(5) χ^2_{red}	(6) qPAH (%)	(7) γ (%)	(8) U_{min}	(9) $\langle U\rangle$	(10) $\log(L_{\mathrm{dust}})$ $(L\odot)$	(11) f_{PDR}
J14234238+3400324	−9.51	10.36	S+S	0.35	5.00 ± 0.79	1.16 ± 0.55	3.22 ± 0.74	3.74	9.67	0.11
J14234632+3401012	−9.76	10.51	S+S	1.60	6.38 ± 0.61	0.61 ± 0.11	1.82 ± 0.61	1.99	9.26	0.06
J14245831−0303597	−9.84	10.31	S+S	1.01	5.16 ± 0.71	0.60 ± 0.06	4.31 ± 1.13	4.66	10.68	0.06
J14295031+3534122	−10.36	10.73	S+S	1.56	1.61 ± 0.43	2.73 ± 0.68	3.90 ± 1.42	5.36	9.91	0.23
J14334683+4004512	−10.12	11.04	S+S	0.53	4.08 ± 0.68	1.44 ± 0.53	1.95 ± 0.52	2.35	10.56	0.14
J14334840+4005392	−9.74	10.62	S+S	0.54	5.04 ± 0.77	0.92 ± 0.48	5.44 ± 1.09	6.12	10.83	0.09
J14442055+1207429	−9.06	10.80	S+S	3.25	0.87 ± 0.24	12.67 ± 3.86	1.17 ± 0.62	3.39	10.19	0.50
J14442079+1207552	−9.77	10.62	S+S	1.02	2.96 ± 0.70	3.30 ± 0.98	2.57 ± 0.63	3.77	10.58	0.26
J15064579+0346214	−10.27	10.91	S+S	0.81	6.32 ± 0.72	2.85 ± 0.80	1.13 ± 0.59	1.61	10.27	0.23
J15101776+5810375	−9.80	10.71	S+S	0.36	4.11 ± 0.60	0.67 ± 0.25	3.17 ± 0.72	3.46	10.27	0.07
J15233768+3749030	−11.24	10.69	S+E	0.45	2.57 ± 1.63	4.84 ± 3.35	2.14 ± 0.98	3.63	9.35	0.33
J15281276+4255474	−9.61	10.60	S+S	0.48	4.09 ± 0.56	0.60 ± 0.05	2.54 ± 0.61	2.76	10.52	0.06
J15523393+4620237	−10.44	10.30	S+E	0.40	6.49 ± 0.57	0.61 ± 0.11	2.12 ± 0.33	2.30	10.56	0.06
J15562191+4757172	−10.18	10.14	S+E	0.21	3.49 ± 0.60	2.14 ± 0.60	2.57 ± 0.63	3.35	9.95	0.19
J15583784+3227471	−10.30	10.94	S+S	0.37	2.90 ± 0.78	0.60 ± 0.03	3.91 ± 0.73	4.23	10.63	0.06
J16024254+4111499	−10.07	10.79	S+S	1.25	4.72 ± 0.83	1.69 ± 0.65	3.32 ± 0.77	4.09	10.77	0.16
J16024475+4111589	−10.70	10.76	S+S	0.28	3.79 ± 0.79	1.53 ± 0.74	3.18 ± 0.68	3.86	10.31	0.15
J16080648+2529066	−10.57	11.11	S+S	13.90	6.63 ± 0.54	2.88 ± 0.77	0.80 ± 0.15	1.15	10.02	0.23
J16082261+2328459	−10.49	10.96	S+S	2.83	5.22 ± 0.65	0.60 ± 0.03	1.57 ± 0.69	1.71	10.19	0.06
J16082354+2328240	−10.21	10.89	S+S	1.88	2.18 ± 0.46	3.16 ± 0.84	4.44 ± 1.65	6.36	10.77	0.25
J16372583+4650161	−10.83	11.16	S+S	4.83	1.26 ± 0.83	8.47 ± 3.21	0.79 ± 0.04	1.82	10.33	0.42
J17045097+3449020	−9.60	10.99	S+S	0.49	3.19 ± 0.82	4.17 ± 1.22	6.68 ± 1.62	10.35	11.38	0.31
J20471908+0019150	−10.83	11.09	S+E	8.29	4.02 ± 0.55	0.60 ± 0.03	0.79 ± 0.04	0.87	9.71	0.06

Note. Description of columns: (1) Galaxy ID taken from 2MASS. (2) log(sSFR) from Cao et al. (2016). (3) Stellar mass. (4) Pair type: S+S or S+E. (5) Reduced χ^2 of model fit. (6) Percentage of dust in PAH form. (7) Percentage of galaxy dust exposed to $U > U_{\mathrm{min}}$. (8) Relative intensity of the diffuse ISRF. (9) Average relative intensity, U, of starlight on dust grains. (10) Luminosity of dust. (11) Fraction of luminosity due to regions with $U > 10^2$.

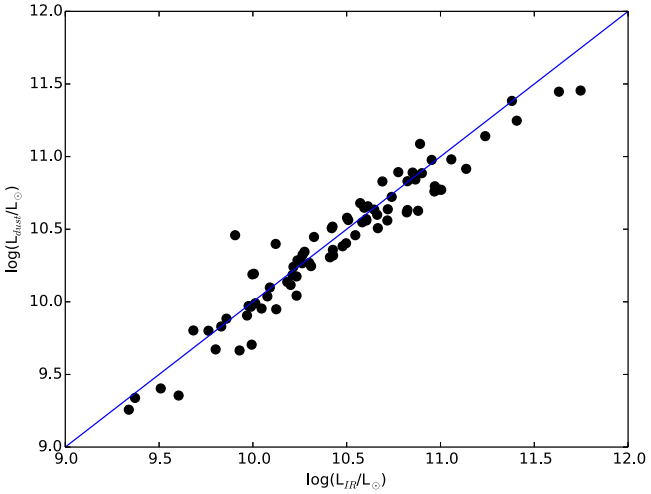

Figure 5. Comparison of the CIGALE L_{dust} to the *Herschel* band derived L_{IR} of Cao et al. (2016). The solid line represents a one-to-one match of the parameters.

9. CORRELATION OF DUST PARAMETERS

In order to investigate the underlying conditions for the DL07 dust parameters, we examine the correlations of U_{min}, qPAH, and γ with respect to each other. Figure 7 shows that there is no significant correlation of the qPAH and U_{min} of any of the samples in our study. It can be seen from Figure 7 that spirals in S+S pairs have the highest U_{min} with the most extreme cases possessing a very low qPAH. Our next comparison of the three DL07 parameters in Figure 9 does not display any significant correlation of γ and U_{min}. Figure 8 illustrates the γ versus qPAH moderate and strong anti-correlations (Spearman $\rho = -0.59, -0.76$) for the spirals in S+S and S+E pairs, respectively. The anti-correlation for the control galaxies is indicated as weak. According to Figure 8 paired spirals have a lower fraction of PAH (as measured by qPAH) when there is a larger fraction of dust heated above U_{min} (as measured by γ). This is similar to the f12/f25 versus f60/f100 anti-correlation for *IRAS* galaxies. Low qPAH control galaxies follow this trend as well but the lack of sample correlation is due to the relatively higher qPAH expressed in the control group.

Enhancements in Cao et al. (2016) are best shown in the sSFR, which may have an influence on the DL07 parameters. There is no significant dependance by the Spearman coefficient of qPAH on the sSFR in Figure 10. It should be noted, however, that there is a population of S+S spirals with high sSFR, which have the lowest qPAH values. These stand as unique among the three samples.

All three samples, spirals in S+S, S+E, and control, show a strong correlation of U_{min} with the sSFR (Figure 11 (Spearman $\rho = 0.68$, 0.67, and 0.59 respectively). The upper range of sSFR and U_{min} is dominated the by S+S spirals, which have the low qPAH values seen in Figure 10.

10. DUST PARAMETER ENHANCEMENTS

In order to determine the enhancement of the parameters that have different distributions from control in Figure 6, we create stellar mass bins as used in Cao et al. (2016). The stellar mass bins are selected as $\log(M_{\mathrm{star}}/M_{\odot}) < 10.4$, $10.4 \leqslant$

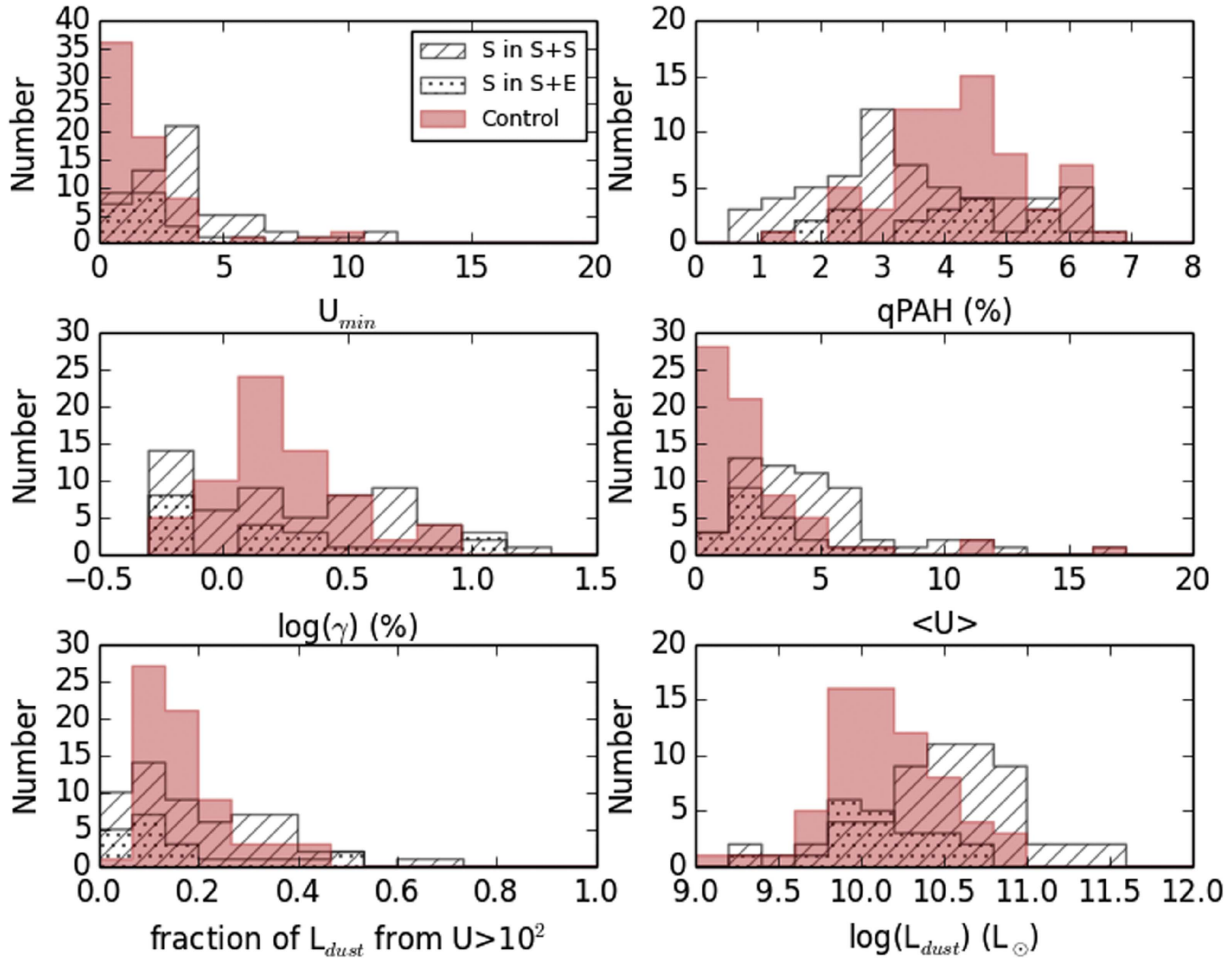

Figure 6. Histograms of the $U_{\rm min}$, qPAH, and γ parameter output of CIGALE for the S+S, S+E, and control samples along with those of the calculated values of $\langle U \rangle$, the fraction of $L_{\rm dust}$ emitted from regions with $U > 10^2$ (known as fPDR), and $L_{\rm dust.}$

$\log(M_{\rm star}/M_\odot) < 10.7$,$10.7 \leqslant \log(M_{\rm star}/M_\odot) < 11.0$, and $\log(M_{\rm star}/M_\odot) \geqslant 11.0$. Errors based on binning are reported as standard errors (standard deviation of the mean) technique. Figure 12 displays the $U_{\rm min}$, qPAH, $\langle U \rangle$, and fPDR for the spirals in S+S, S+E, and control samples. All four parameters for the S+E spirals are within the errors of the control sample. However, in contrast to the S+E pairs, the $U_{\rm min}$ in S+S spirals significantly exceeds that of the control sample and the S+E in the three upper mass bins. The parameter $U_{\rm min}$ is correlated to the overall dust temperature, $T_{\rm dust}$, based on a power-law relationship presented in the literature with varying but similar conversion factors (Aniano et al. 2012; Hunt et al. 2015).

The qPAH and $\langle U \rangle$ of S+S spirals are also seen to be significantly different from the parameters of the control in the same three upper mass bins as the excess in $U_{\rm min}$. The qPAH is lower than both other samples but only significantly against the control. $\langle U \rangle$ exceeds both that of the spirals in S+E and control. The values of fPDR only differ in the lowest mass bin for S+S spirals versus both other samples. There are no overall correlations of any of these parameters with stellar mass. The ϵ enhancements are defined as the difference of values averaged over all mass bins and their corresponding averages for the control sample (Table 3). The enhancements of $U_{\rm min}$, $\langle U \rangle$, and reduction of qPAH in the S+S pairs is in sharp contrast to the similarity of the S+E to the control sample.

11. SUMMARY AND DISCUSSION

We present a CIGALE analysis of the dust parameters defined in the DL07 dust models for a sample of close major-merger galaxy pairs. The sample morphology is both spiral–spiral (S+S) and spiral–elliptical (S+E), allowing for a probe into the interaction physics and its influence on dust. The contributions (qPAH) of PAH grains to the dust mass, fraction (γ) of dust from PDR to the total dust, and the minimum intensity ($U_{\rm min}$) from the interstellar radiation field (ISRF) are analyzed along with their secondary related parameters such as mean radiation intensity, $\langle U \rangle$, and dust luminosity (total and in PDRs).

Elbaz et al. (2011) demonstrate the contribution of the diffuse ISM templates as compared to star-forming templates within the GOODS-*Herschel* survey. The corresponding ISM $\langle U \rangle$, $T_{\rm eff}$, and fPAH (the PAH-to-total mass fraction; compare to qPAH) are given as 1.8, 19 K, and 8.74%, respectively. Star-forming regions are respectively measured as having $\langle U \rangle$, $T_{\rm eff}$, and fPAH as 757, 53 K, and 1.38%. Galaxies exhibit a mixture of the two templates and our H-KPAIR parameters give us the ability to assess the relative importance of the ISM and star-forming regions to our paired spirals. The Elbaz et al. (2011) analysis would imply that the H-KPAIR spirals in S+S pairs have the largest fraction of star-forming regions based on temperature, $\langle U \rangle$, and qPAH as seen in Figure 12 among our samples.

Table 2
K–S Test Distribution Statistics

	$P_{U\min}$	$P_{\rm qPAH}$	P_{γ}	$P_{\langle U\rangle}$	$P_{\rm fPDR}$	$P_{L\rm dust}$
S+S versus Control	2.3×10^{-7}	5.5×10^{-5}	0.041	6.1×10^{-7}	0.023	1.6×10^{-5}
S+E versus Control	0.081	0.522	0.079	0.010	0.079	0.997
S+S versus S+E	0.005	0.146	0.614	0.012	0.614	0.002

Note. The K–S test significance P for distribution similarity of each of the histograms in Figure 6 vs. the other samples as described in column 1.

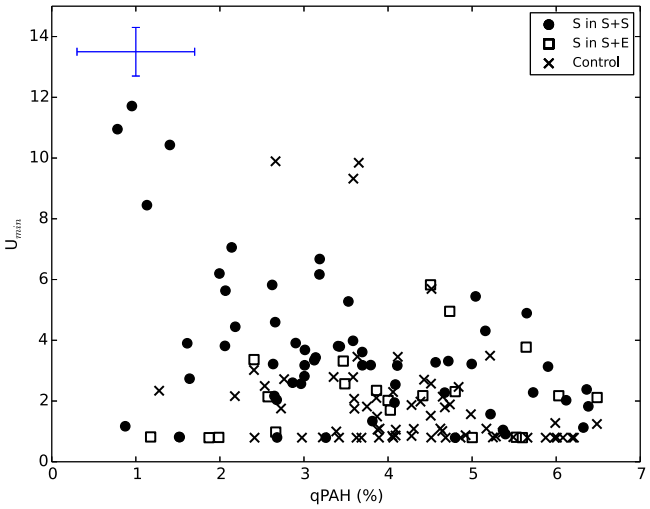

Figure 7. $U_{\rm min}$ vs. qPAH for the galaxy samples including spirals in S+S (circles), S+E (squares), and the control galaxies (crosses). The blue error bars indicate the average error for each parameter.

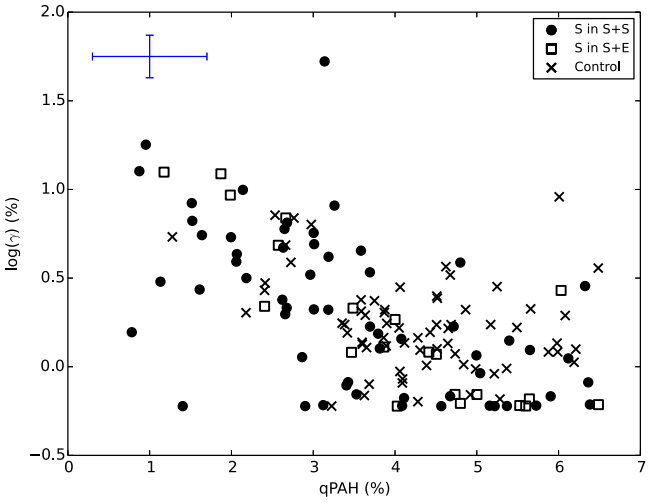

Figure 8. log(γ (%)) vs. qPAH for the galaxy samples including spirals in S+S (circles), S+E (squares), and the control galaxies (crosses). The blue error bars indicate the average error for each parameter.

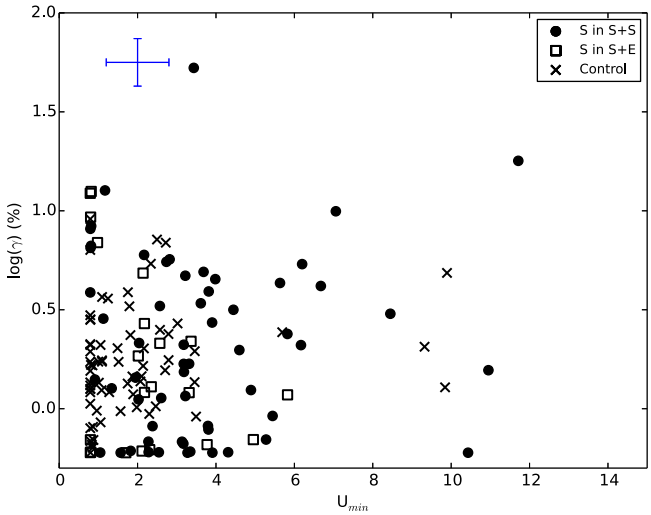

Figure 9. log(γ (%)) vs. $U_{\rm min}$ for the galaxy samples including spirals in S+S (circles), S+E (squares), and the control galaxies (crosses). The blue error bars indicate the average error for each parameter.

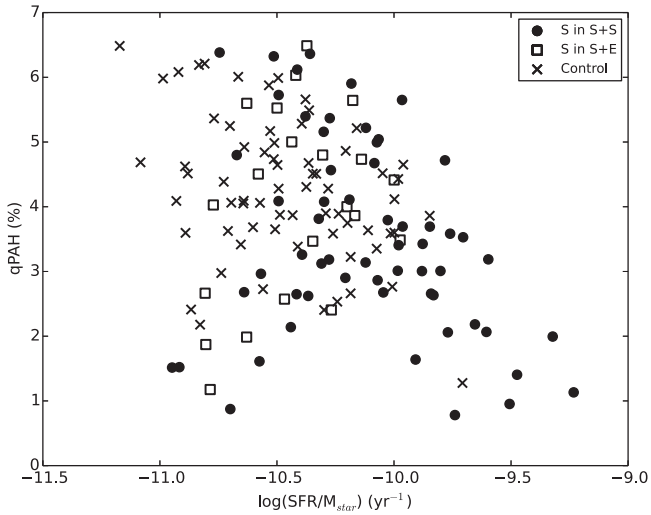

Figure 10. qPAH as a function of sSFR for spirals in S+S (circles), S+E (squares), and the control galaxies (crosses).

Any display of smaller qPAH such as the reduction seen in the S+S pairs is likely a PAH deficiency due to enhanced interstellar radiation fields (ISRF) from star formation in the pair environment (Contursi et al. 2000; Engelbracht et al. 2005; Madden et al. 2006; Cook et al. 2014). The main-sequence of galaxies (Elbaz et al. 2011) have a log(sSFR) ~ -9.6 with star-bursting galaxies defined as log(sSFR) ~ -9.3. Nordon et al. (2012) demonstrate that the difference in sSFR from the expected main-sequence (Elbaz et al. 2011) of galaxies (ΔsSFR$_{\rm MS}$) is a determinant in the relative strength of the luminosity at 8 μm, which diminishes at higher ΔsSFR$_{\rm MS}$. The 8 μm range contains the PAH feature measured in the corresponding *Spitzer*/IRAC band and a reduced qPAH would likely be a measurable result of the same physical environment. The population of S+S spirals has an enhanced ΔsSFR$_{\rm MS}$ according to their sSFR enhancement (Cao et al. 2016). Since qPAH is diminished for a population of these spirals with log (sSFR) > -10 (Figure 10), it is likely a reflection of the same shift in SED shape as seen in Nordon et al. (2012), which is interpreted as the result of more compact star-forming regions

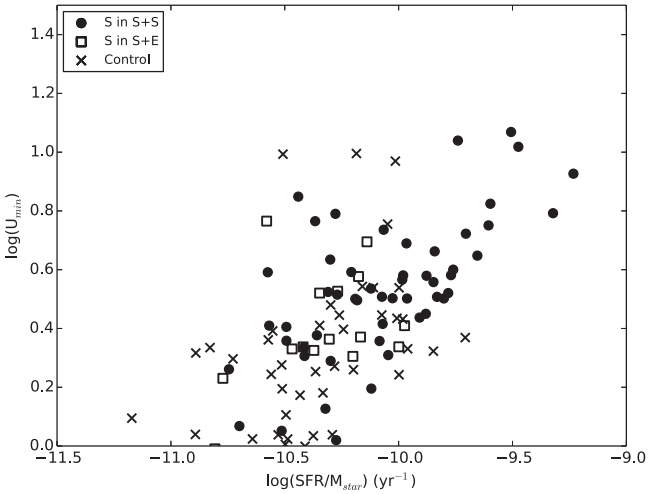

Figure 11. log($U_{\rm min}$) as a function of sSFR for spirals in S+S (circles), S+E (squares), and the control galaxies (crosses).

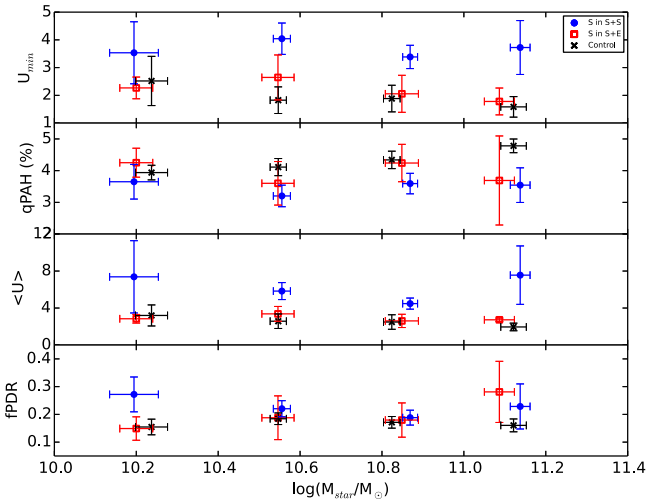

Figure 12. The $U_{\rm min}$, qPAH, $\langle U\rangle$, and fPDR for the galaxy samples including spirals in S+S (blue circles), S+E (red squares), and the control galaxies (black crosses). Galaxies are into divided into four mass bins and error bars represent the standard error.

Table 3
Dust Parameter Enhancements

Sample	$\epsilon_{U\rm min}$	$\epsilon_{\rm qPAH}$	$\epsilon_{\langle U\rangle}$	$\epsilon_{\rm fPDR}$
S+S	1.72 ± 0.55	−0.79 ± 0.33	3.19 ± 1.13	0.04 ± 0.03
S+E	0.29 ± 0.54	−0.25 ± 0.46	0.31 ± 0.65	0.02 ± 0.04

(Elbaz et al. 2011). The low-qPAH galaxy examples have sSFR that falls in range from main-sequence to just below that of the star-bursting definition. The "compactness" defined in Elbaz et al. (2011) refers to an overall measure of the extended versus non-extended location of star-bursting and not to the details of the size of individual regions or PDRs. So despite an indication of more compact star formation, the γ parameter shows a strong anti-correlation with qPAH (Figure 8) in these same galaxies, an indication of a larger fraction of dust heated above the diffuse ISM temperature.

The similarity of the spirals in the S+E pairs to control spirals indicates a difference in the interaction physics or history of the S+E pairs when compared to S+S pairs. Possible conditions that could cause the lack of enhancement are the presence of multiple star-forming mechanisms in S+S pairs such as torque-induced gas flow as well as cloud–cloud interactions and turbulence (Bournaud 2011; Renaud et al. 2014). The S+E pairs either only have the torque induced mechanism at their disposal because of the lack of two gas-rich environments or because the presence of a hot intergalactic medium (IGM) associated with the elliptical suppresses the star formation, or both suppression conditions are present.

This publication makes use of data products from the *Wide-field Infrared Survey Explorer*, which is a joint project of the University of California, Los Angeles, and the Jet Propulsion Laboratory/California Institute of Technology, funded by the National Aeronautics and Space Administration. The *Herschel* spacecraft was designed, built, tested, and launched under a contract to ESA managed by the *Herschel*/Planck Project team by an industrial consortium under the overall responsibility of the prime contractor Thales Alenia Space (Cannes), and including Astrium (Friedrichshafen), responsible for the payload module and for system testing at spacecraft level, Thales Alenia Space (Turin), responsible for the service module, and Astrium (Toulouse), responsible for the telescope, with an excess of a hundred subcontractors. C.C. is supported by NSFC-11503013, NSFC-11420101002, and NSFC-10978014. We would also like to thank the anonymous reviewer for improvements to this manuscript.

REFERENCES

Adelman-McCarthy, J. K., Agüeros, M. A., Allam, S. S., et al. 2007, ApJS, 172, 634
Alonso-Herrero, A., Ramos Almeida, C., Esquej, P., et al. 2014, MNRAS, 443, 2766
Aniano, G., Draine, B. T., Calzetti, D., et al. 2012, ApJ, 756, 138
Barton, E. J., Arnold, J. A., Zentner, A. R., Bullock, J. S., & Wechsler, R. H. 2007, ApJ, 671, 1538
Barton, E. J., Geller, M. J., & Kenyon, S. J. 2000, ApJ, 530, 660
Bournaud, F. 2011, in EAS Publications Series, Vol. 51, Star Formation in the Local Universe – EES2010, ed. C. Charbonnel & T. Montmerle, 107
Brinchmann, J., Abraham, R., Schade, D., et al. 1998, ApJ, 499, 112
Bundy, K., Fukugita, M., Ellis, R. S., et al. 2009, ApJ, 697, 1369
Bundy, K., Fukugita, M., Ellis, R. S., Kodama, T., & Conselice, C. J. 2004, ApJL, 601, L123
Burkert, A. 2006, CRPhy, 7, 433
Cao, C., Xu, C. K., Domingue, D., et al. 2016, ApJS, 222, 16
Ciesla, L., Boquien, M., Boselli, A., et al. 2014, A&A, 565, A128
Cluver, M. E., Jarrett, T. H., Hopkins, A. M., et al. 2014, ApJ, 782, 90
Cole, S., Norberg, P., Baugh, C. M., et al. 2001, MNRAS, 326, 255
Conselice, C. J., Bershady, M. A., Dickinson, M., & Papovich, C. 2003, AJ, 126, 1183
Contursi, A., Lequeux, J., Cesarsky, D., et al. 2000, A&A, 362, 310
Cook, D. O., Dale, D. A., Johnson, B. D., et al. 2014, MNRAS, 445, 899
Cutri, R. M., et al. 2014, yCat, 2328, 0
Dale, D. A., Aniano, G., Engelbracht, C. W., et al. 2012, ApJ, 745, 95
Darg, D. W., Kaviraj, S., Lintott, C. J., et al. 2010, MNRAS, 401, 1043
Dasyra, K. M., Tacconi, L. J., Davies, R. I., et al. 2006, ApJ, 638, 745
Di Matteo, P., Bournaud, F., Martig, M., et al. 2008, A&A, 492, 31
Domingue, D. L., Xu, C. K., Jarrett, T. H., & Cheng, Y. 2009, ApJ, 695, 1559
Draine, B. T., Dale, D. A., Bendo, G., et al. 2007, ApJ, 663, 866
Draine, B. T., & Lee, H. M. 1984, ApJ, 285, 89
Draine, B. T., & Li, A. 2007, ApJ, 657, 810
Eisenstein, D. J., Weinberg, D. H., Agol, E., et al. 2011, AJ, 142, 72
Elbaz, D., Dickinson, M., Hwang, H. S., et al. 2011, A&A, 533, A119
Elmegreen, D. M., Kaufman, M., Brinks, E., Elmegreen, B. G., & Sundin, M. 1995, ApJ, 453, 100
Engelbracht, C. W., Gordon, K. D., Rieke, G. H., et al. 2005, ApJL, 628, L29
Erwin, P. 2015, ApJ, 799, 226
Griffin, M. J., Abergel, A., Abreu, A., et al. 2010, A&A, 518, L3

Helou, G., Lu, N. Y., Werner, M. W., Malhotra, S., & Silbermann, N. 2000, ApJL, 532, L21
Hopkins, P. F., Hernquist, L., Cox, T. J., et al. 2006, ApJS, 163, 1
Hunt, L. K., Draine, B. T., Bianchi, S., et al. 2015, A&A, 576, A33
Hwang, H. S., Elbaz, D., Dickinson, M., et al. 2011, A&A, 535, A60
Jarrett, T. H., Chester, T., Cutri, R., et al. 2000, AJ, 119, 2498
Jarrett, T. H., Cohen, M., Masci, F., et al. 2011, ApJ, 735, 112
Jarrett, T. H., Masci, F., Tsai, C. W., et al. 2012, AJ, 144, 68
Jarrett, T. H., Masci, F., Tsai, C. W., et al. 2013, AJ, 145, 6
Kauffmann, G., White, S. D. M., & Guiderdoni, B. 1993, MNRAS, 264, 201
Kennicutt, R. C., Jr., Roettiger, K. A., Keel, W. C., van der Hulst, J. M., & Hummel, E. 1987, AJ, 93, 1011
Kroupa, P. 2001, MNRAS, 322, 231
Laher, R. 2012, APT: Aperture Photometry Tool, Astrophysics Source Code Library, ascl:1208.003
Lang, D. 2014, AJ, 147, 108
Lang, D., Hogg, D. W., & Schlegel, D. J. 2014, arXiv:1410.7397
Larson, R. B., & Tinsley, B. M. 1978, ApJ, 219, 46
Madden, S. C., Galliano, F., Jones, A. P., & Sauvage, M. 2006, A&A, 446, 877
Maraston, C. 2005, MNRAS, 362, 799
Masci, F. J., & Fowler, J. W. 2009, in ASP Conf. Ser. 411, Astronomical Data Analysis Software and Systems XVIII, ed. D. A. Bohlender, D. Durand, & P. Dowler (San Francisco, CA: ASP), 67
Mateos, S., Alonso-Herrero, A., Carrera, F. J., et al. 2012, MNRAS, 426, 3271
Mathis, J. S., Rumpl, W., & Nordsieck, K. H. 1977, ApJ, 217, 425
Moon, J.-S., & Yoon, S.-J. 2015, PKAS, 30, 469
Noll, S., Burgarella, D., Giovannoli, E., et al. 2009, A&A, 507, 1793
Nordon, R., Lutz, D., Genzel, R., et al. 2012, ApJ, 745, 182
O'Donnell, J. E., & Mathis, J. S. 1997, ApJ, 479, 806
Oliver, S. J., Bock, J., Altieri, B., et al. 2012, MNRAS, 424, 1614
Ott, S. 2010, in ASP Conf. Ser. 434, Astronomical Data Analysis Software and Systems XIX, ed. Y. Mizumoto, K.-I. Morita, & M. Ohishi (San Francisco, CA: ASP), 139
Park, C., & Choi, Y.-Y. 2009, ApJ, 691, 1828
Park, C., Gott, J. R., III, & Choi, Y.-Y. 2008, ApJ, 674, 784
Pilbratt, G. L., Riedinger, J. R., Passvogel, T., et al. 2010, A&A, 518, L1
Poglitsch, A., Waelkens, C., Geis, N., et al. 2010, A&A, 518, L2
Renaud, F., Bournaud, F., Kraljic, K., & Duc, P.-A. 2014, MNRAS, 442, L33
Rieke, G. H., Young, E. T., Engelbracht, C. W., et al. 2004, ApJS, 154, 25
Roche, P. F., Aitken, D. K., Smith, C. H., & Ward, M. J. 1991, MNRAS, 248, 606
Roehlly, Y., Burgarella, D., Buat, V., et al. 2012, in ASP Conf. Ser. 461, Astronomical Data Analysis Software and Systems XXI (San Francisco, CA: ASP), 569
Roehlly, Y., Burgarella, D., Buat, V., et al. 2014, in ASP Conf. Ser. 485, Astronomical Data Analysis Software and Systems XXIII, ed. N. Manset & P. Forshay (San Francisco, CA: ASP), 347
Scudder, J. M., Ellison, S. L., Torrey, P., Patton, D. R., & Mendel, J. T. 2012, MNRAS, 426, 549
Skrutskie, M. F., Cutri, R. M., Stiening, R., et al. 2006, AJ, 131, 1163
Stern, D., Assef, R. J., Benford, D. J., et al. 2012, ApJ, 753, 30
Toomre, A., & Toomre, J. 1972, ApJ, 178, 623
Traficante, A., Calzoletti, L., Veneziani, M., et al. 2011, MNRAS, 416, 2932
Wright, E. L., Eisenhardt, P. R. M., Mainzer, A. K., et al. 2010, AJ, 140, 1868
Xu, C., & Helou, G. 1996, ApJ, 456, 163
Xu, C., & Sulentic, J. W. 1991, ApJ, 374, 407
Xu, C. K., Domingue, D., Cheng, Y.-W., et al. 2010, ApJ, 713, 330
Xu, C. K., Shupe, D. L., Béthermin, M., et al. 2012, ApJ, 760, 72
York, D. G., Adelman, J., Anderson, J. E., Jr., et al. 2000, AJ, 120, 1579